Machine learning techniques for damage detection in wind turbine blades

Bernardo Henrique Santos Lopes
bernardo.lopes@tecnico.ulisboa.pt

Instituto Superior Técnico, Universidade de Lisboa, Portugal

December 2021

Abstract

Damage detection plays a vital role in the operation of machinery and represents one of the greatest challenges in the mechanical, aerospace, and aeronautical industries. The wind energy industry, where wind turbines are subjected to enormous mechanical and aerodynamic loads and extreme environmental conditions during operation, is one of the industries that can benefit most from this kind of study. The installation of wind turbines requires significant investments over a long period concerning maintenance and repairs. In order to reduce these costs and guarantee the integrity and longevity of such structures, the use of a reliable structural health monitoring system coupled with a robust anomaly detection methodology is crucial to assess the viability of the investments during their lifespan. Regarding the subsequent fault detection, numerous machine learning and deep learning techniques have succeeded in a broad range of applications. This thesis aims to implement algorithms capable of consistently detecting and assessing faults in two wind turbine blades of different materials. Such techniques as multivariate Gaussian anomaly detection and anomaly detection autoencoders were successfully incorporated by recognising deviating patterns from the healthy state to its damaged state in experimentally acquired data such as modal parameters and frequency response functions. These vibration-based data were obtained through modal shaker testing, modal hammer testing and pull-and-release testing applying experimental modal analysis and operational modal analysis.

Keywords: damage detection, wind turbine blade, modal analysis, structural health monitoring, machine learning.

1. Introduction

1.1 Motivation

1.1.1 Wind energy

The wind is one of the most appealing renewable energy sources for electricity production, representing a significant part of the power generation mix in some countries. For example, in 2017, wind energy in Portugal accounted for 21.6% of total electric energy production, covering 24.6% of the annual electricity demand [17]. Wind energy currently meets 15% of EU electricity demand; by 2030, it is expected to cover 30% of demand and employ 569,000 people [14].

1.1.2 Wind turbines

Wind turbine blades are not only subject to mechanical and aerodynamic loads during operation but also extreme environmental conditions such as gusts, icing and lightning strikes. The main reasons for wind turbine (WT) damage are thermal cycling, sand, bird impacts, leading and trailing edge erosion, fatigue, moisture intrusion, and mechanical failure [14]. The installation of WTs requires significant investments during a minimum of a 20-year lifespan. To assess the reliability of the investments during this period, the use of structural health monitoring (SHM) systems to continuously monitor the condition of WTs is crucial. SHM can provide relevant information for rescheduling maintenance tasks and lowering its associated costs. The maintenance of wind turbine blades involves visual inspection, which can be dangerous and time-consuming. Regular WT *Operation and Maintenance* (O&M) costs are very high, accounting for 20–25% of the total *levelized cost of energy* (LCOE) over the turbine's lifetime. Therefore, developing a remote blade condition monitoring system is a topic that the industry is engaged in.

1.2 Topic overview

1.2.1 Damage detection

Damage detected early on can prevent irreversible structural failures, hence the importance of a ro-

bust defect detection methodology for ensuring machinery's structural integrity and operational safety while lowering maintenance and repair costs. Reliable damage detection techniques are a significant challenge in the mechanical, aerospace, and aeronautical industries. In particular, for the WT industry, due to the high magnitude of the structures and respective investments [4, 3].

1.2.2 Structural health monitoring

Structural health monitoring (SHM) refers to a reliable system capable of detecting and evaluating adverse changes in a structure due to damage, or regular operation [13, 21]. One way of carrying out this monitoring process is through the extraction and analysis of vibration-based data [16, 17].

1.2.3 Modal analysis

A general process of SHM based on these methods involves collecting relevant vibration response data. Damaged structures will have these modal parameters affected due to local discontinuity created by the fault [8, 10, 19]. Experimental modal analysis (EMA) is a typical technique for estimating the modal properties of structures that have been used for many years. This technique assumes that the user knows both inputs and outputs; however, it is not always possible to measure both, particularly in operational conditions. For this reason, the operational modal analysis (OMA) technique was then introduced. The OMA approach serves the same goals as the EMA, but it is more suitable for operating machines because it relies only on measured outputs and does not need to know about the input forces. The estimation of OMA parameters combined with a proper SHM strategy can be used to track unusual system variations and inform when unplanned maintenance service is required.

1.2.4 Machine learning

In recent years, advanced computational artificial intelligence algorithms have achieved large success in detecting different types of faults [2, 7].

1.2.5 Deep learning

Deep learning (DL) is a subset of ML mainly focused on artificial neural network algorithms. DL goes a step further in terms of complexity and power, representing more complex architectures and algorithms. Remarkable progress has been made in the field of DL with emerging applications for SHM [23, 11] and damage detection. In particular for damage detection algorithms using autoencoders [15, 12, 20]. Also, deep neural networks are being implemented in the mechanical and aerospace industries, for instance, in the damage detection of beam structures, [1], damage assessment in rotating machinery and motor fault detection [22, 9]. Studies have also been done for WT fault classification [18] and autonomous crack detection [5].

1.3 Objectives

- Understand the principles of modal analysis and perform it using state-of-the-art software;
- Conduct experimental campaigns to collect vibration-based data from the blades;
- Explore different ML approaches to build a reliable and fully automatic damage detection model;
- Study which experimentally collected features are more relevant to the performance of fault detection;
- Compare the developed fault detection algorithms based on accuracy, sensibility and damage assessment capability;
- Assess the applicability of the developed models in a real-world scenario.

2. Background

2.1 Modal analysis

Modal analysis is a technique for examining a structure and estimating its dynamic properties such as natural frequencies, damping ratios, and mode shapes [6]. Almost all real-world situations can be modelled as systems with more than one degree of freedom (DOF).

2.2 Multiple degrees of freedom systems

In the time domain, the equation of motion for an MDOF system is the same as the equation of motion for an SDOF system, but it is a matrix equation:

$$[m]\{\ddot{x}\} + [c]\{\dot{x}\} + [k]\{x\} = \{f\} \tag{1}$$

Where $[m]$ is the mass matrix, $[c]$ the damping matrix and $[k]$ the stiffness matrix of the system. These matrices have n x n dimension. The vector $x(t)$ represents the displacement as a function of the time, and $f(t)$ is the excitation of the system also as a function of the time. Both have n x 1 dimension. The equation of motion can be transformed into the Laplace domain by assuming that all initial displacements and velocities are zero for all degrees of freedom:

$$([m]s^2 + [c]s + [k])\{X(s)\} = \{F(s)\} \quad \text{or;} \tag{2}$$

$$[Z(s)]\{X(s)\} = \{F(s)\} \tag{3}$$

The dynamic stiffness matrix is represented by $[Z(s)]$. Inverting this equation results in:

$$\{X(s)\} = [H(s)]\{F(s)\} \tag{4}$$

Where $[H(s)]$ is the *transfer function matrix* because it represents the ratio of the system's response

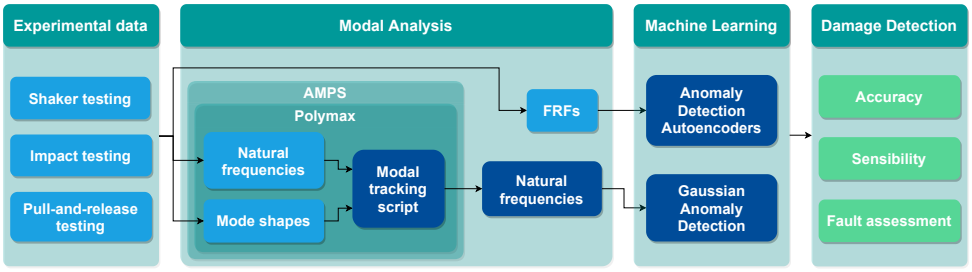

Figure 1: Thesis overview schema.

to the corresponding force input in the Laplace domain for each DOF. This matrix contains functions with complex values. The *system characteristic equation* is the determinant of $[Z(s)]$, and its roots are the *system poles*, defining the values of the natural frequencies of the system. The solution for this problem is based on the eigenvalues of a matrix, so the first step is to define the equation 3 in the general eigenvalue problem formulation. Considering:

$$[\mathrm{A}]=\begin{bmatrix}[0] & [m]\\ [m] & [c]\end{bmatrix} \quad ; \quad [\mathrm{B}]=\begin{bmatrix}-[m] & [0]\\ [0] & [k]\end{bmatrix} \tag{5}$$

$$\{\mathrm{Y}\}=\begin{bmatrix}s\{X\}\\ \{X\}\end{bmatrix} \quad ; \quad \{\mathrm{F'}\}=\begin{bmatrix}\{0\}\\ \{F\}\end{bmatrix} \tag{6}$$

While also taking into consideration that:

$$(s[m]-s[m])\{X\}=\{0\} \tag{7}$$

$$(s[A]+[B])\{Y\}=\{F'\} \tag{8}$$

Equation 8 is the general formulation for the eigenvalue problem when the *force vector* is null. The system's eigenvalues (λ_r, with $r=1,...,n$) are the solutions of the equation 9, calculated for s.

$$\left|s[A]+[B]\right|=0 \tag{9}$$

The number of solutions of this equation is determined by the system's degree of freedom, n. In complex conjugate pairs, there are $2n$ complex-valued eigenvalues. The *damping factor* is the real component of a pole, and the *damped natural frequency* is the imaginary part, as in the SDOF systems. Each of the system's eigenvalues is associated with an eigenvector named *mode shape vector*, $\{\psi\}_r$ Like the system poles, they appear in complex conjugate pairs. The modal vectors contain complex-valued modal displacements, and the phase of these displacements might differ between elements. On the equation 3 these vectors make the *force vector* null by definition. The transfer function can also be represented in terms of the system poles since they are the roots of the system characteristic equation:

$$[H(s)]=\frac{\mathrm{adj}([Z(s)])}{\prod_{r=1}^{n}E\,(s-\lambda_r)\,(s-\lambda_r^*)} \tag{10}$$

$$=\frac{\mathrm{adj}([Z(s)])}{\prod_{r=1}^{2n}E\,(s-\lambda_r)} \tag{11}$$

Where E is a constant. Regarding SDOF systems, the partial fraction expansion theory can be applied to the expression 11 to obtain the *residues*, A_r. The following equation relates them to the *mode shape vectors*. For each residue:

$$[A]_r=Q_r\{\psi\}_r\{\psi\}_r^t \tag{12}$$

Since the *residues* $[A]_r$ are absolute quantities, it is possible to deduce from the equation 12 that the modal vectors are vectors with a scaling factor $[A]_r$. Each column j of the matrix $[A]$ has enough information to produce that matrix unless it coincides with a modal coefficient ψ_{jr} equal to zero. This occurs because all the columns are proportional to one another, but if the coefficient is 0, the corresponding row and column will be zero. As a result, if the excitation point is in a nodal point of one mode, that mode will not be recognised in experimental modal analysis. The FRF matrix should be obtained by evaluating the transfer function matrix along the frequency axis:

$$[\mathrm{H(j\ }\omega)]=\sum_{r=1}^{n}\left(\frac{Q_r\{\psi\}_r\{\psi\}_r^t}{(j\omega-\lambda_r)}+\frac{Q_r^*\{\psi\}_r^*\{\psi\}_r^{*t}}{(j\omega-\lambda_r^*)}\right) \tag{13}$$

The matrix $[H(j\omega)]$ has complex values and depends on the input frequency, so its values are not constants. Taking into account that the FRF is defined as the output-to-input ratio. When an excitation F_k is applied on k DOF, $H_{jk}(\omega)$ is the response X_j for the j DOF. The input force and the system response (measured in displacement, velocity, or acceleration) are quantifiable. As a result, the equation 13 can be used to find the system's modal parameters. As previously stated, the FRF of a MDOF system is the sum of the FRFs of n SDOF systems.

3. Implementation

3.1 Modal parameter estimation

3.1.1 Titanium wind turbine blade

Given the high stiffness of the titanium blade, the impact testing had the best performance because it was the only test capable of exciting all ten modes highlighted in figure 2 for the analysed bandwidth of 0-800 Hz. For this following analysis of natural frequencies and damping ratios, the FRFs used were obtained from the impact testing and considering

only the bandwidth of 15-800 Hz since it was the configuration that presented the best results for this blade, as explained above. Figure 2 shows the stabilisation diagram with the system poles obtained for a model size of 50 from the Polymax tool of the Simcenter Testlab. Ten reference normal modes represented in the figure were selected based on the stable poles, each corresponding to a peak of the sum of the 30 FRFs from the ten tri-axial accelerometers. The modal parameters presented in table 1 correspond to the average natural frequencies and damping ratios of all healthy experimental runs.

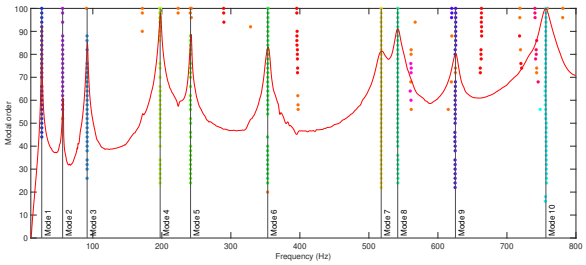

Figure 2: Ti blade stabilization diagram clustered with representative poles.

The mode-set selected was compared to itself in the calculated Auto-MAC in figure 3. Ideally, each mode should be uniquely observed and have a different shape than the other modes. What can be observed in the figure, where all the non-diagonal values of the matrix have correlations below 30%.

Table 1: Ti blade modal parameters.

Mode	Natural frequency [Hz]	Damping ratio
1	25.969	0.67%
2	56.187	0.89%
3	92.050	0.91%
4	197.803	1.00%
5	241.526	0.97%
6	353.559	0.99%
7	517.906	0.99%
8	541.696	0.86%
9	625.627	0.65%
10	756.772	0.89%

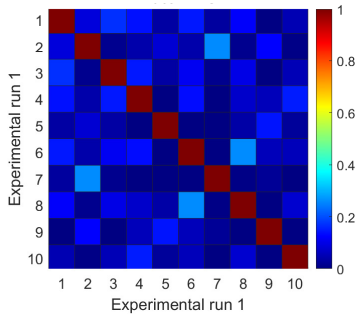

Figure 3: Auto-MAC for a healthy experimental run of the Ti blade.

Having been defined the reference modes and the respective natural frequencies of the structure in the healthy state, the comparison with the damaged state will be made. In the following figure 5, it is represented in blue the frequency range of all the healthy experimental runs performed with the respective mean, minimum and maximum values represented by dashed lines. All points represented correspond to frequencies from damaged experimental runs, organised by position on the blade and magnitude of the mass used.

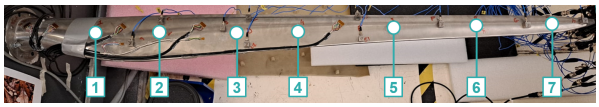

Figure 4: Mass positions used to perform the damaged experimental runs of the Ti blade.

The first evident conclusion is the deviation from the healthy reference frequencies for all masses tested for all the normal modes. The second interesting conclusion to be drawn from the first two modes of Ti is the almost linear increase of the frequency shift according to the increase of the mass's distance to the clamped side of the blade and the magnitude of the mass itself. This phenomenon only does not apply to the lowest magnitude mass of 15.5g, which, despite having sufficient magnitude to cause an observable deviation, does not have sufficient magnitude to cause a relevant deviation on par with the other masses so that any pattern can be observed. The same tendency occurs until the

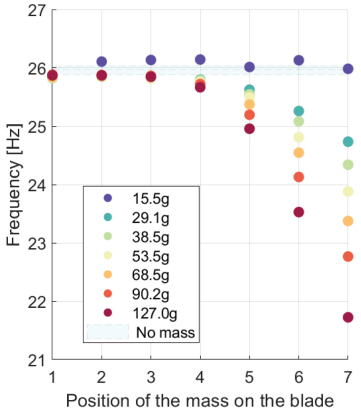

Figure 5: Natural frequencies of the 1st mode of the Ti blade.

fourth mode, from which the increase in the frequency shift is no longer related to the position of the mass in the structure and increases only with the increment of magnitude. For high-order modes the frequency distribution starts to be purely random.

3.1.2 GFRP wind turbine blade

Both the impact and the shaker testing were able to detect the fourteen normal modes depicted in fig-

ure 8; however, the modal shaker was the one that did so most consistently throughout all the experimental runs. Figure 7 depicts the clear distinction

Figure 6: Mass positions used to perform the damaged experimental runs of the GFRP blade.

between the experimental runs carried out with the GFRP blade in both healthy and damaged states.

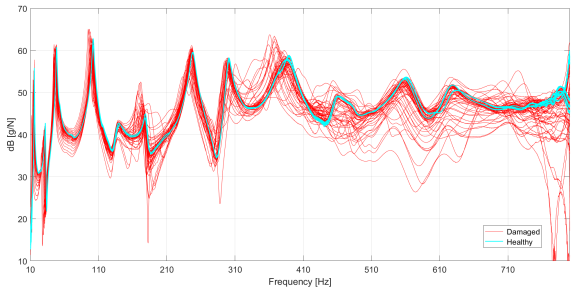

Figure 7: GFRP blade FRFs from healthy vs damaged experimental runs.

The GFRP blade was experimentally tested for the same frequency spectrum as the Ti Blade (0-800Hz) to allow for comparisons between the two under similar circumstances. However, given the entirely different nature of the two, the GFRP blade starts presenting inconsistencies for the higher frequencies of the bandwidth. For this reason, only a smaller, more reliable portion of the spectrum was considered henceforth. The FRFs used to find the eigenfrequencies and damping ratios of the GFRP blade were obtained from the modal shaker testing. Figure 8 shows the stabilisation diagram, for the 10-650 Hz bandwidth, with the system poles obtained for the model size of 50, where 14 reference modes were selected based on the stable poles, each corresponding to a peak of the sum of the FRFs.

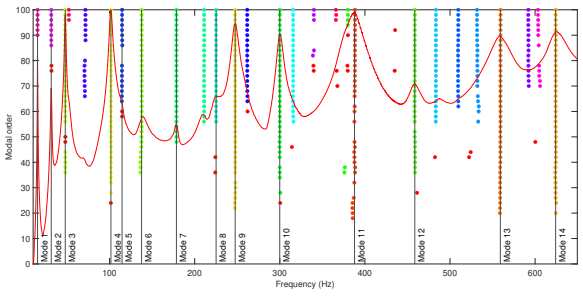

Figure 8: GFRP blade stabilization diagram clustered with representative poles.

The modal parameters presented in table 2 correspond to the average natural frequencies and damping ratios of all healthy experimental runs. The mode-set selected was compared to itself in the calculated Auto-MAC in figure 9. After selecting the

Table 2: GFRP blade modal parameters.

Mode	Natural frequency [Hz]	Damping ratio
1	15.346	0.83%
2	31.437	1.73%
3	47.890	1.51%
4	101.485	1.41%
5	114.879	2.41%
6	137.672	4.47%
7	178.737	1.53%
8	225.382	2.72%
9	247.519	1.50%
10	299.862	1.14%
11	388.350	2.01%
12	457.484	2.02%
13	560.414	2.38%
14	626.092	2.36%

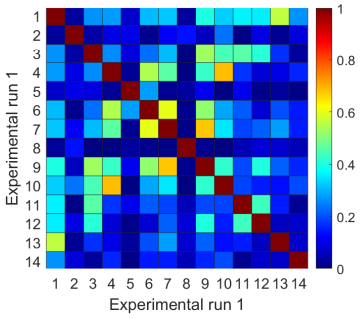

Figure 9: Auto-MAC for a healthy experimental run of the GFRP blade.

reference modes of the healthy state, the comparison to the damaged frequencies can now be made. As seen for the titanium blade, for the GFRP blade, it is also possible to confirm the deviation of the damaged frequencies from the blue frequency band corresponding to the healthy experimental runs.

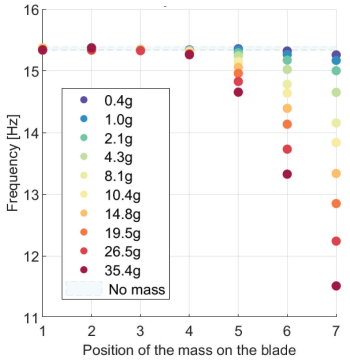

Figure 10: Natural frequencies of the 1st mode of the GFRP blade.

This deviation is evident for all the masses, including the smaller percentage ones not analysed for the titanium blade. However, this deviation is only evident for most of the masses in positions five onwards, which correspond to the last third of the blade, near the tip. The second conclusion about the increase of this deviation with the approach of the mass to the tip and the increase of the mass magnitude, which was verified for the Ti blade, is

also verifiable for the GFRP blade. The fact that more mass magnitudes were analysed for this blade highlights, even more, this linear correlation of the frequency shift with the mass magnitude and with the mass position, as it is possible to observe in figure 10. This tendency, similar to the GFRP blade, is verified until the fourth mode, where the correlation happens only with the increase in magnitude and for high-order modes there is no longer any correlation.

3.2 Multivariate Gaussian anomaly detection

The idea behind this methodology is based on the natural frequency shift of a damaged structure in relation to its healthy state. Therefore the premise is: if the algorithm can learn the natural frequencies of a structure in its undamaged state, it should be able to detect divergent frequencies of the same structure and consider them as anomalies. As portrayed in the diagram of figure 13, the algorithm starts by reading the files from each experimental run, in the damaged and undamaged state separately, containing the natural frequencies of the blade.

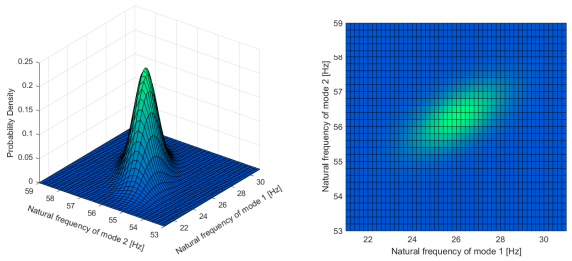

Figure 11: Multivariate Gaussian distribution applied to the natural frequencies of the first two normal modes of the Ti blade.

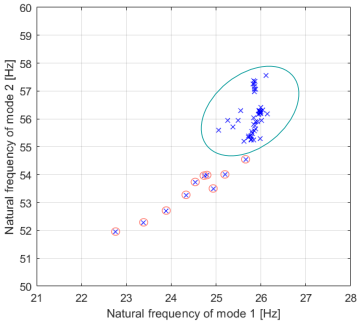

Figure 12: MGAD classification applied to the natural frequencies of the first two normal modes of the Ti blade.

Each file corresponds to an experimental run containing the eigenfrequencies for every mode. The process of quantifying how divergent a natural frequency should be to be considered an outlier was done using a multivariate Gaussian distribution. For the implementation within the scope of this thesis, the features used to perform the multivariate Gaussian distribution were the natural frequencies of all the modes for each blade. A visual representation of this approach can be seen in figures 11 and 12.

3.3 Anomaly detection autoencoders

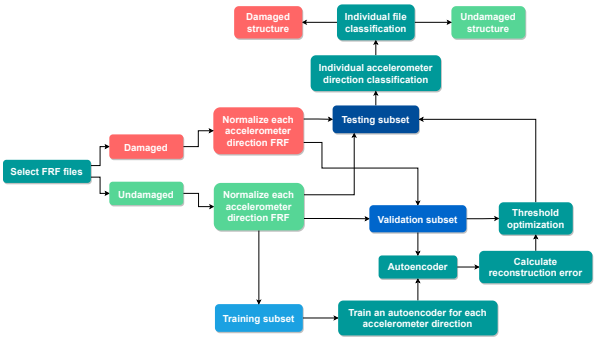

Figure 14: ADAE methodology diagram.

Another technique developed was the Anomaly Detection Autoencoder (ADAE). The ADAE is a semi-supervised learning approach that involves training the algorithm with normal features, i.e. data from the structure in its healthy state and then classifying the rest of the testing dataset based on its reconstruction error. If the error of a certain point exceeds an established threshold, it is classified as an anomaly. As schematically shown in the diagram of figure 14, the algorithm starts by reading the files from each experimental run, in the damaged and undamaged state separately, containing the FRFs from the blade. Each experimental run file has data from the three directions (x, y and z) of each accelerometer. Considering that ten accelerometers were used, there are three times ten FRFs, i.e. 30 per experimental run. Then, the data are normalised along the accelerometer directions to reduce the experimentally inevitable differences in data acquisition from run to run. After that, the data from the selected files are divided into three subsets. The first one, consisting of one-third of the healthy data, is used for the training of the AEs. An AE is trained for each direction of each accelerometer. The second subset containing one-third of healthy data and half of the damaged data is used for the validation process - finding the optimal threshold. Finally, the last subset, also consisting of half of the damaged data and one-third of the undamaged data is used for testing - classifying the files based on the threshold found. In figure 15 is illustrated the fundamental principle of an AE applied to our use case. At the top of the diagram, in green, it is represented the input signal corresponding to an FRF in the healthy state and the respective AE reconstruction, which exhibits an almost perfect reconstruction, originating only residual error. While at the bottom, in red, the input signal

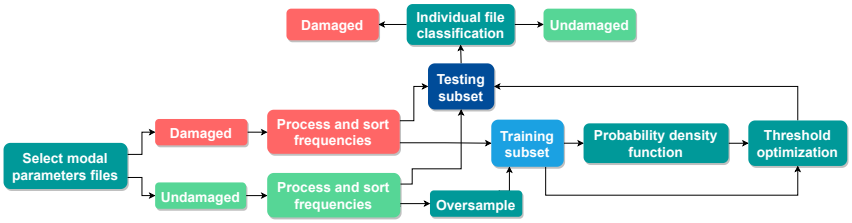

Figure 13: MGAD methodology diagram.

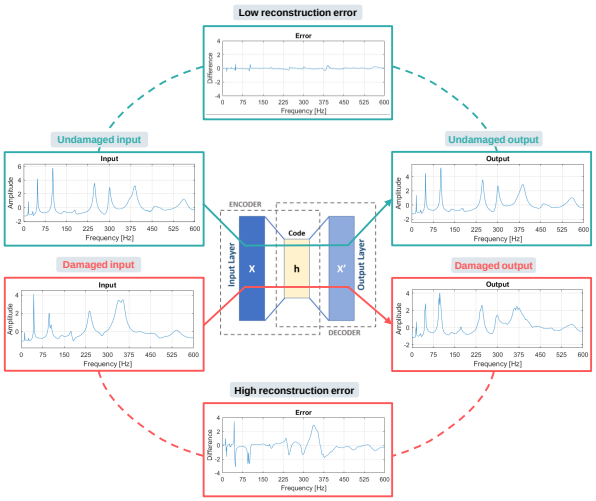

Figure 15: ADAE reconstruction error principle.

of the structure in its damaged state manifests a significant difference in the AE reconstruction and corresponding error. For this thesis algorithm implementation, the root-mean-square error (RMSE) was used to estimate the reconstruction error.

$$\text{RMSE}=\sqrt{\sum_{i=1}^{n}\frac{(\hat{y}_i-y_i)^2}{n}} \tag{14}$$

The following figure 16 show the reconstructions of the FRFs of the structure in its healthy state, and it is visible that the reconstruction is near perfect; i.e., the output FRF is roughly the same as the input FRF.

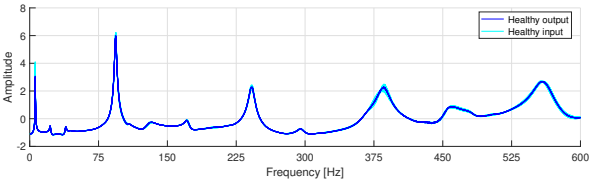

Figure 16: ADAE FRF reconstructions for healthy inputs from the GFRP blade.

While in figure 17, it is represented the case for the input FRFs of the structure in its damaged state, and the difference in their reconstruction is evident and significant. In order to give an insight into the distribution of the reconstruction error along the spectral lines of the FRF, i.e. along its bandwidth, figure 18 show the RMSE between all the collected experimental runs and their respective

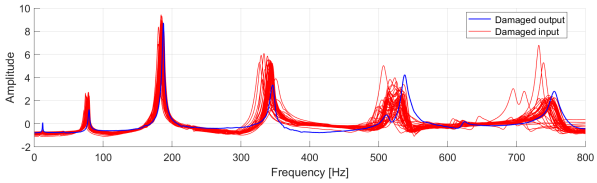

Figure 17: ADAE FRF reconstructions for damaged inputs from the Ti blade.

output reconstructions for the damaged and healthy state separately. As expected, it is possible to notice the RMSE corresponding to undamaged data remaining approximately null the whole spectrum. In contrast, the damaged data part remains significant over the whole bandwidth, with the largest spikes in the zones near the natural frequencies of the blade in its original state. The graphs in figures 19 and 20 shows the variation of RMSE over the different experimental runs for both healthy and damaged data. Analogously to what was observed in section 3.1, where the natural frequencies of the damaged structure presented a larger deviation for higher magnitude and masses closer to the tip of the blade, the same applies to the reconstruction error of the AEs. It can be seen that for the titanium

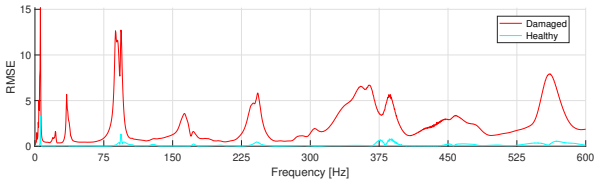

Figure 18: Sum of the reconstruction RMSE from every healthy vs damaged experimental run for one of the accelerometer directions of the GFRP blade.

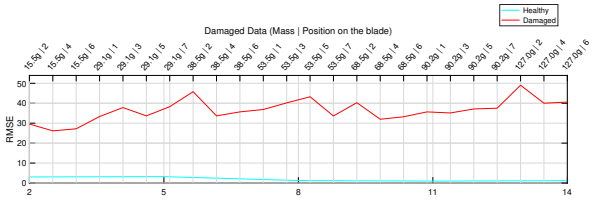

Figure 19: RMSE for the different experimental runs of the Ti blade.

turbine blade, it is quite simple to define a threshold value between the errors of the healthy and damaged structure due to the large difference between the two. Regarding the GFRP turbine blade, the

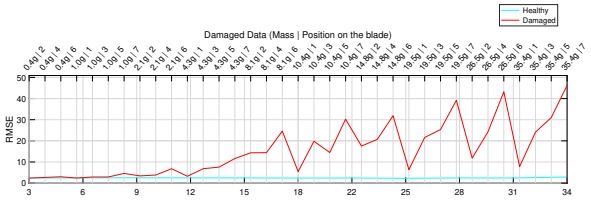

Figure 20: RMSE for the different experimental runs of the GFRP blade.

same is true but only for masses above 4.3g, corresponding to 0.6% of the blade mass. For the algorithm to be able to identify damage below those magnitudes, the thresholding process addressed in the following subchapter has to be taken into account. The selection of the reconstruction error threshold, which defines what points are considered faults, is one of the most significant challenges when using ADAEs. For each possible threshold, a corresponding value of true positives and false positives exists. To facilitate the study of the threshold selection considering both variables at the same time, a score based on the intersection over Union (IoU) method defined in equation 15 was used. The automatic threshold selection process was based on the maximum value of this parameter.

$$IoU = \frac{TP}{TP + FN + FP} \tag{15}$$

4. Results

4.1 Multivariate Gaussian Anomaly Detection

4.1.1 GFRP turbine blade

In table 3, it is presented the sensitivity study of the algorithm's damage detection as a function of the mentioned variables. On the left are the intervals of masses, and in opposition, are the intervals of mass positions (figure 4) considered to reach the corresponding accuracy. For instance, the first column of the first row of the table corresponds to the algorithm's accuracy when running, considering all the damaged experimental runs of the, in other words, every combination of magnitude and position of the mass. Since the tests were performed with ten different mass magnitudes in seven different positions, the algorithm ran with seven times ten, i.e. 70 different files, representing 70 experimental runs of the blade in the damaged state. On the other hand, the entry of the last column of the last row corresponds to the algorithm's accuracy, taking only into consideration the experimental run with the mass of 35.4g at position 7. As seen in chapter 3.1, defects in positions closer to the free extremity of the blade and higher magnitude lead to higher frequency shifts. The opposite is true for natural frequencies from experimental runs with mass positions closer to the clamped side and lower magnitude, with insufficient variation in comparison with its healthy state. This

Table 3: MGAD accuracies for the different combinations of intervals of magnitude and position of the GFRP blade.

Mass [g]	Position of the mass on the blade						
	1 to 7	**2 to 7**	**3 to 7**	**4 to 7**	**5 to 7**	**6 to 7**	**7**
0.4 to 35.4	94.1%	97.8%	95.1%	94.4%	93.8%	92.6%	100.0%
1.0 to 35.4	95.7%	97.7%	94.7%	94.1%	93.3%	92.3%	100.0%
2.1 to 35.4	95.5%	97.5%	94.4%	93.8%	93.1%	92.0%	100.0%
4.3 to 35.4	95.0%	100.0%	100.0%	100.0%	100.0%	91.7%	100.0%
8.1 to 35.4	94.6%	100.0%	100.0%	100.0%	100.0%	91.3%	100.0%
10.4 to 35.4	93.9%	100.0%	100.0%	100.0%	100.0%	90.9%	100.0%
14.8 to 35.4	93.3%	100.0%	100.0%	100.0%	100.0%	90.5%	100.0%
19.5 to 35.4	92.6%	100.0%	100.0%	100.0%	100.0%	90.0%	100.0%
26.5 to 35.4	91.3%	100.0%	100.0%	100.0%	100.0%	89.5%	100.0%
35.4	100.0%	100.0%	100.0%	100.0%	100.0%	100.0%	100.0%

damaged frequency shift will strongly influence the thresholding process. A high-frequency shift will result in a more optimal threshold, whereas a low-frequency shift will result in a poor threshold, which will be reflected in the algorithm's accuracy. The results obtained shown in table 3 validate this reasoning.

4.1.2 Titanium turbine blade

As seen for the GFRP WT blade, the worst performances are noticed when considering masses of 0.4, 1.0 and 2.1 grams, which correspond to a maximum of 0.3% of the GFRP blade's mass. The titanium WT blade was only tested for masses as light as 0.6% of its total weight. For this reason, given the results for the GFRP blade, it makes sense that the results for the Ti blade would be close to the perfect accuracy, as was the case for the GFRP blade for most combinations of runs above 0.3% of the total mass. Which was verified.

4.2 Anomaly detection autoencoders

Contrary to what was seen regarding MGAD, this algorithm was able to achieve perfect accuracy for certain configurations when analysing the entire dataset of masses tested. Thus, those configurations, i.e. AE architectures, will be presented, and the most optimal for each of the WT blades will be ascertained. The algorithm architecture and the tuning of its hyperparameters is one aspect that significantly impacts its accuracy. The two hyperparameters that most affected the final output of the algorithm were the *code size* and the maximum number of *epochs*. An epoch is a term used in ML that indicates the number of times that the learning algorithm will work through the entire training dataset, and the *code size* represents the number of neurons in the hidden layer, i.e. the number of nodes in the middle layer.

4.2.1 GFRP turbine blade

In table 4, it is shown the study performed for these two parameters and how they influenced the accuracy of the algorithm concerning the GFRP blade

data. Taking into account that the algorithm execution time and its computational requirements increase with the increasing of the hyperparameters, i.e., along the lines and columns of table 4, a preselection of the four configurations, which presented perfect accuracy for the less computational impact possible, was made.

Table 4: Accuracy comparison of the algorithm architectures.

Epochs	Code size							
	1	5	10	20	30	40	50	60
1	97.8%	91.3%	95.7%	89.1%	93.5%	95.7%	93.5%	93.5%
2	95.7%	95.7%	87.0%	87.0%	89.1%	91.3%	89.1%	91.3%
3	97.8%	91.3%	87.0%	87.0%	87.0%	87.0%	91.3%	87.0%
4	91.3%	91.3%	89.1%	89.1%	87.0%	91.3%	87.0%	87.0%
5	89.1%	89.1%	91.3%	91.3%	87.0%	93.5%	87.0%	93.5%
10	93.5%	91.3%	91.3%	91.3%	97.8%	97.8%	97.8%	91.3%
15	100.0%	97.8%	100.0%	97.8%	97.8%	97.8%	97.8%	97.8%
20	95.7%	100.0%	100.0%	97.8%	100.0%	100.0%	95.7%	97.8%
30	100.0%	100.0%	100.0%	97.8%	100.0%	100.0%	100.0%	97.8%
50	100.0%	100.0%	100.0%	100.0%	100.0%	100.0%	100.0%	100.0%
100	100.0%	100.0%	100.0%	100.0%	100.0%	100.0%	100.0%	100.0%
200	100.0%	100.0%	97.8%	100.0%	100.0%	100.0%	100.0%	100.0%
300	97.8%	100.0%	100.0%	100.0%	100.0%	100.0%	100.0%	100.0%
500	100.0%	100.0%	100.0%	100.0%	100.0%	100.0%	100.0%	100.0%
800	100.0%	97.8%	100.0%	100.0%	100.0%	100.0%	100.0%	100.0%
1000	100.0%	100.0%	100.0%	100.0%	100.0%	100.0%	100.0%	100.0%

4.2.2 Titanium turbine blade

Considering that the ADAEs results were favourable for the GFRP WT blade when analysing all the tested masses, the same results were expected for the titanium WT blade since the masses used in this blade tests were heavier, meaning they would be easier to detect. This was confirmed with the perfect accuracy results obtained considering all the masses and using the minimal configuration of 1 Epoch and Modal Size 1; the fastest and less computationally demanding type of AE possible. Therefore, optimisation analysis as the one done for GFRP blade architecture is not necessary for the Ti blade.

5. Conclusions

After all the research work developed throughout this thesis, it was concluded that implementing ML techniques concerning damage detection on vibration-based data was successful. The conclusions about the results obtained can be structured according to the two algorithms developed: MGAD and ADAEs. Regarding the MGAD, its initial premise centred on the variation of natural frequencies of a damaged structure was confirmed. However, with regard to the GFRP blade, this frequency variation was insufficient for mass positions closer to the clamped side of the blade and lower magnitude masses. The heavy reliance on precise modal parameter estimation is a drawback of MGAD. Concerning the ADAEs results, it can be concluded that its premise, based in the variation of the FRF of a damaged structure, was verified and proven to be quite reliable, enabling the algorithm to detect all the masses tested in every position of the two blades. The only aspect to consider that affects the algorithm's performance is the architecture and the optimisation of the hyperparameters.

References

[1] O. Avci, O. Abdeljaber, S. Kiranyaz, and D. Inman. Structural damage detection in real time: implementation of 1d convolutional neural networks for shm applications. In *Structural Health Monitoring & Damage Detection*, volume 7, pages 49–54. Springer, 2017.

[2] J. Chatterjee and N. Dethlefs. Scientometric review of artificial intelligence for operations & maintenance of wind turbines: The past, present and future, 7 2021.

[3] X. Chen, S. Semenov, M. McGugan, S. Hjelm Madsen, S. Cem Yeniceli, P. Berring, and K. Branner. Fatigue testing of a 14.3 m composite blade embedded with artificial defects – Damage growth and structural health monitoring. *Composites Part A: Applied Science and Manufacturing*, 140, 1 2021.

[4] F. L. dos Santos, B. Peeters, H. Van der Auweraer, L. C. Góes, and W. Desmet. Vibration-based damage detection for a composite helicopter main rotor blade. *Case Studies in Mechanical Systems and Signal Processing*, 3:22–27, 6 2016.

[5] C. V. Dung et al. Autonomous concrete crack detection using deep fully convolutional neural network. *Automation in Construction*, 99:52–58, 2019.

[6] D. J. Ewins. *Modal Testing: Theory, Practice and Application*. John Wiley Sons, 2nd edition, 2009.

[7] C. R. Farrar and K. Worden. *Structural health monitoring: a machine learning perspective*. John Wiley & Sons, 2012.

[8] G. R. Gillich, Z. I. Praisach, M. Abdel Wahab, and O. Vasile. Localization of transversal cracks in sandwich beams and evaluation of their severity. *Shock and Vibration*, 2014, 2014.

[9] O. Janssens, V. Slavkovikj, B. Vervisch, K. Stockman, M. Loccufier, S. Verstockt, R. Van de Walle, and S. Van Hoecke. Convolutional neural network based fault detection for rotating machinery. *Journal of Sound and Vibration*, 377:331–345, 2016.

[10] G. C. Larsen, P. Berring, D. Tcherniak, H. Nielsen, K. Branner, and K. B. Effect. Effect of a Damage to Modal Parameters of a Wind Turbine Blade. Technical report, 2014.

[11] Y. Lei, F. Jia, J. Lin, S. Xing, and S. X. Ding. An Intelligent Fault Diagnosis Method Using Unsupervised Feature Learning Towards Mechanical Big Data. *IEEE Transactions on Industrial Electronics*, 63(5):3137–3147, 5 2016.

[12] C. Lu, Z. Y. Wang, W. L. Qin, and J. Ma. Fault diagnosis of rotary machinery components using a stacked denoising autoencoder-based health state identification. *Signal Processing*, 130:377–388, 1 2017.

[13] M. Martinez-Luengo, A. Kolios, and L. Wang. Structural health monitoring of offshore wind turbines: A review through the Statistical Pattern Recognition Paradigm, 10 2016.

[14] M. McGugan and L. Mishnaevsky. Damage mechanism based approach to the structural health monitoring of wind turbine blades. *Coatings*, 10(12):1–23, 12 2020.

[15] M. S. Minhas and J. Zelek. Semi-supervised Anomaly Detection using AutoEncoders. 2020.

[16] G. Oliveira, F. Magalhães, Cunha, and E. Caetano. Continuous dynamic monitoring of an onshore wind turbine. *Engineering Structures*, 164:22–39, 6 2018.

[17] G. Oliveira, F. Magalhães, Cunha, and E. Caetano. Vibration-based damage detection in a wind turbine using 1 year of data. *Structural Control and Health Monitoring*, 25(11), 11 2018.

[18] A. Shihavuddin, X. Chen, V. Fedorov, A. Nymark Christensen, N. Andre Brogaard Riis, K. Branner, A. Bjorholm Dahl, and R. Reinhold Paulsen. Wind turbine surface damage detection by deep learning aided drone inspection analysis. *Energies*, 12(4):676, 2019.

[19] Y. Wang, M. Liang, and J. Xiang. Damage detection method for wind turbine blades based on dynamics analysis and mode shape difference curvature information. *Mechanical Systems and Signal Processing*, 48(1-2):351–367, 10 2014.

[20] L. Wen, L. Gao, and X. Li. A new deep transfer learning based on sparse auto-encoder for fault diagnosis. *IEEE Transactions on Systems, Man, and Cybernetics: Systems*, 49(1):136–144, 1 2019.

[21] W. Yang, Z. Peng, K. Wei, and W. Tian. Structural health monitoring of composite wind turbine blades: Challenges, issues and potential solutions. *IET Renewable Power Generation*, 11(4):411–416, 2017.

[22] W. Zhang, C. Li, G. Peng, Y. Chen, and Z. Zhang. A deep convolutional neural network with new training methods for bearing fault diagnosis under noisy environment and different working load. *Mechanical Systems and Signal Processing*, 100:439–453, 2018.

[23] R. Zhao, R. Yan, Z. Chen, K. Mao, P. Wang, and R. X. Gao. Deep learning and its applications to machine health monitoring, 1 2019.